LETTER

A Rational Approach to Improve the Overall Performances of Semitransparent Perovskite Solar Cells by Electrode Optical Management

Antonella Lorusso, Sofia Masi,* Claudia Triolo, Fabrizio Mariano, Simone Muia, Alessandro Cannavale, Yu Duan, Marco Anni, Maria Luisa De Giorgi, Salvatore Patané, Olfa Selmi, Iván Mora-Seró, Stefano De Leo,* and Marco Mazzeo*

Cite This: *ACS Energy Lett.* 2024, 9, 1923−1931

Read Online

ACCESS | Metrics & More | Article Recommendations | Supporting Information

ABSTRACT: Improving the overall characteristics of semitransparent solar cells (STSCs) is a very hard goal, not only because the absorption and the transmission of light through the device are two competitive processes but also because the power conversion efficiency (PCE) decreases with the angle of incidence of sunlight rays due to Fresnel law limits. Here, unprecedented single-junction perovskite STSCs have been fabricated thanks to rational management of the transverse magnetic and electric light reflection modes of a dielectric/metal/dielectric triple layer used as a top electrode. This approach allows an increase of the photocurrent density in a broad angular range of the sunlight incidence and the overall figure of merit of different kinds of perovskite-based solar cells including PCE and light utilization efficiency (LUE), as well as aesthetic properties such as the color rendering index (CRI) and CIELab chromaticity coordinates, thus showing a universal method for real building integration and agrivoltaic applications.
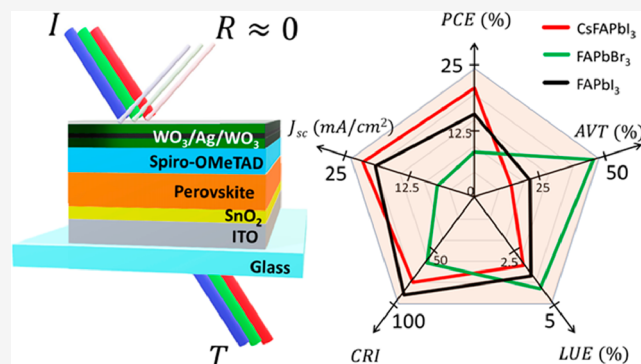
In recent years, the power conversion efficiency (PCE) of perovskite solar cells has shown an exponential increase, reaching values over 26% due to their unique optical and electrical properties that merge a high absorption coefficient with a high carrier diffusion length.[1,2] Moreover, due to the easy tuning of the band gap (from 1.6 to 2.3 eV), halide-perovskite materials are attracting more interest also for the development of semitransparent solar cells (STSCs) integrated in the windows of buildings and skyscrapers.[3,4] This new generation of devices may provide future green electricity, reducing significantly the greenhouse emissions and decoupling the energy production from the energy distribution currently based on expensive electrical grids.[5] Agrivoltaics, wearable electronics, and automobiles are other sectors where perovskite−STSCs can find interesting applications.[6] To characterize the effectiveness of a STSC to transmit visible light, an average visible transmittance (AVT) value ranging from 15% for highly tinted glass up to 90% for clear glass, a color rendering index (CRI) larger than 85, chromaticity coordinates (CIELab a^*, b^*) in the range of $-5 < a^* < 1$ and $-5 < b^* < 5$, and a CIE1931xy color space around ($x = 0.3$, $y = 0.3$) are considered acceptable in residential windows

applications.[7,8] Moreover, the color difference between the normal and off-viewing angle should be minimized to prevent color variations when buildings are viewed at a distance. Nevertheless, as stated by the upper theoretical Shockley−Queisser (SQ) limit,[9] the absorption, on which the photovoltaic effect is based, and transmission are two competitive processes, making the achievement of such a goal very hard, especially for no-wavelength-selective semitransparent solar cells (NWS-STSCs). To account for such a limit, another figure of merit is the light utilization efficiency (LUE), defined as the product PCE × AVT. In NWS-STSCs, the SQ limit imposes a LUE upper limit of 7.5 and 6.5% for an AVT of about 50 and 30%, respectively.[7,9] Several strategies have been pursued to increase the AVT, such as (i) making the active

1923
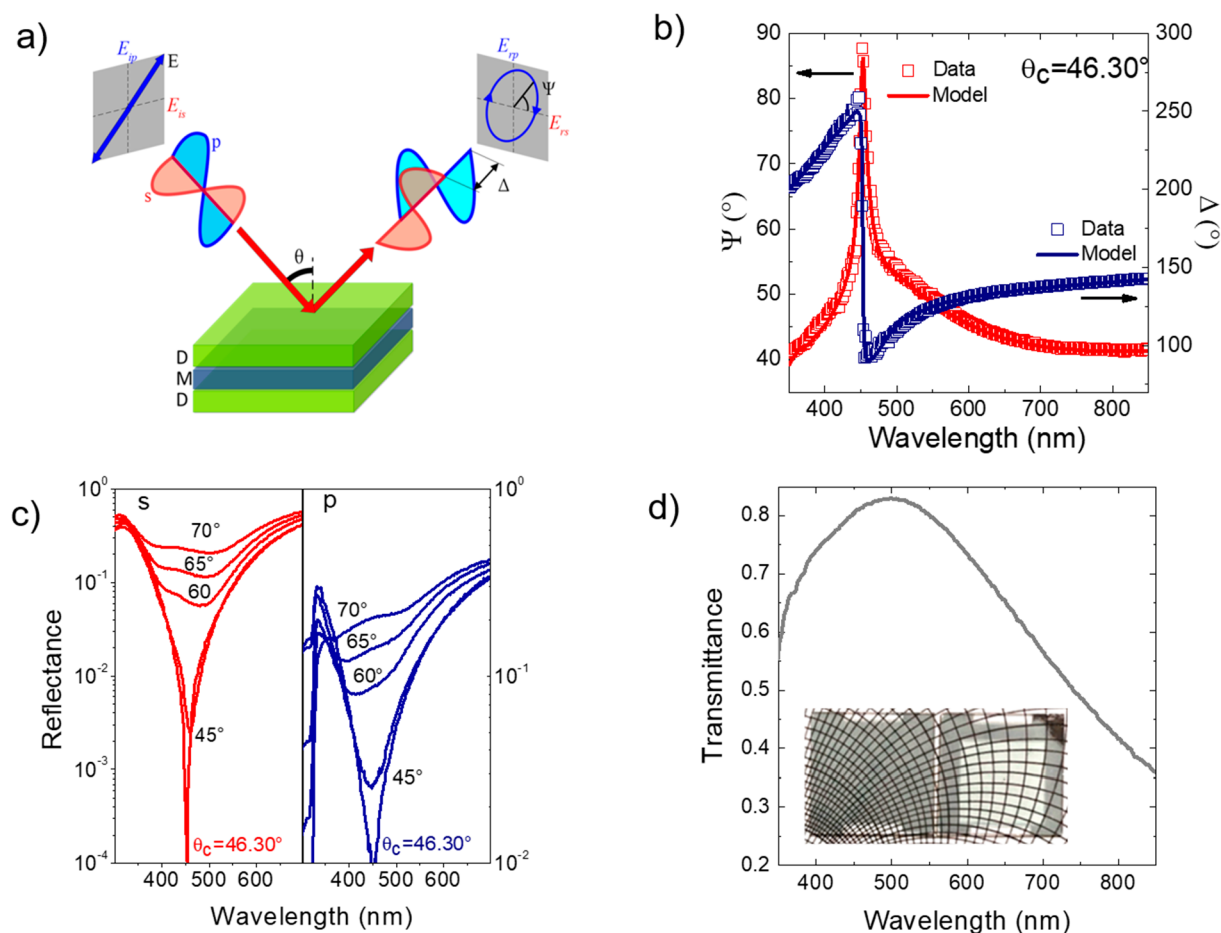
Figure 1. (a) Working scheme of VASE. (b) Ellipsometry data at θ_c for DMD40. (c) s and p mode spectra at different angles of incident light. (d) Transmittance spectrum of DMD40 and picture of the dielectric/metal (on the left) and the DMD40 electrode (on the right).

layers thinner,[4] (ii) reducing the perovskite coverage of the substrate,[10−14] and (iii) employing low reflecting electrodes such as low-dimensional materials or highly doped transparent semiconductors.[15−23] Nevertheless, these strategies in general are expensive, unfriendly for the environment, and produce instability or even damage of the perovskite layer.[16,22,24] Moreover, an improvement of the AVT results in a general reduction of the PCE, thus affecting the LUE. Electrodes based on a combination of layered materials with different optoelectronic characteristics and functionalities have been recently developed with the aim to increase both the PCE and AVT. Among them, three-layered dielectric/metal/dielectric (DMD) thin film sequences, exploiting different combinations of materials, have been deeply explored in real devices.[25−30] Nowadays, the best performances have been reached using an $MoO_3/Au/MoO_3$ architecture as the top electrode in a mixed based perovskite device, with a PCE of 12% and an AVT of 35%,[31] thus achieving a LUE of 4.2%. In an unmixed $FAPbI_3$-based perovskite, a PCE of 15.3% and an AVT of 12.2% (LUE = 1.86%) have been reported using an $MoO_3/Ag/WO_3$ architecture.[25] Nevertheless, all these values are lower than the benchmark required by the market in real building applications, and no studies about the dependence of the device performances on the light incident angle have been reported.

Despite the several developed configurations, full control of the electromagnetic wave propagation through such layered materials, thus guaranteeing rational design of the electrode, is still demanding. Recently, an analytical approach limited only to propagation of light normal to the DMD surface has been developed disregarding the role of the transversal electric (TE or s) and magnetic (TM or p) modes at different angles of incidence due to the difficulty in finding analytical solutions.[32] However, this issue is a key point in practical photovoltaic applications, such as building-integrated photovoltaic windows.[33]

In the present work, we studied the propagation of light through a $WO_3/Ag/WO_3$-DMD electrode by the variable-angle ellipsometric spectroscopy (VASE) technique,[34] with the aim to engineer STSCs satisfying antireflection conditions in a wide angular range of incident light. Since the impact of the contact on the device stability is a common issue in the frame of solar cell architectures with DMD,[35] the system $WO_3/Ag/WO_3$ has been selected due to the low sheet resistance of ∼10 Ω/sq,[30,36] a WO_3 work function of 4.8 eV[37] that efficiently extracts holes, and low diffusion of Ag compared to other metals like Au or Cu through the dielectric, ensuring good device stability.[35] To demonstrate the universality of such an approach, we implemented the optimized DMD structure in two kinds of single-junction semitransparent unmixed solar cells based on cesium formamidinium-lead-iodide ($Cs_{0.1}FA_{0.9}PbI_3$), and formamidinium-lead-bromide ($FAPbBr_3$) perovskites. Remarkable PCE values of 21.2% at an AVT of 15% and 8.9% at an AVT of 48.1% have been reached for $CsFAPbI_3$ and $FAPbBr_3$, respectively, the highest so far achieved for such materials. We realized also $FAPbI_3$-based
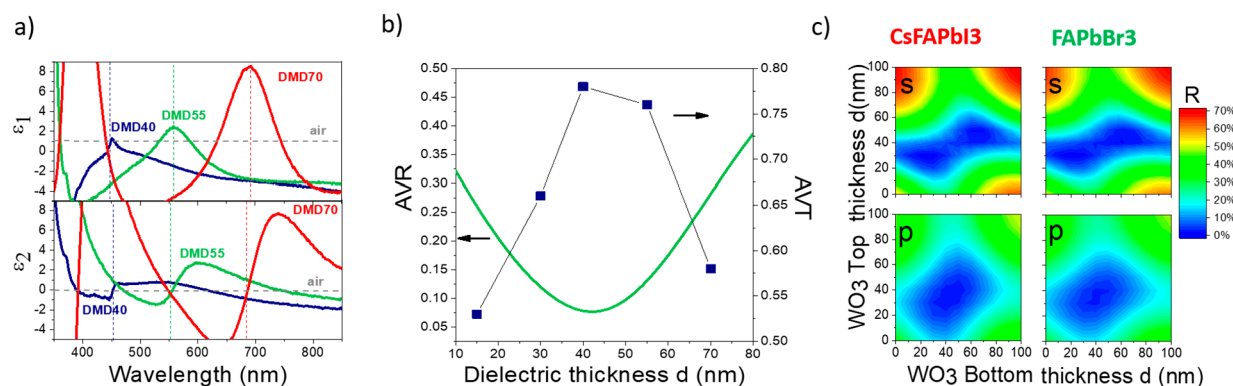
Figure 2. (a) Real (top) and imaginary (bottom) parts of the complex pseudodielectric function at critical angle θ_c. (b) Theoretical AVR and experimental AVT vs the dielectric thickness. (c) Reflectance intensity maps for s and p modes at $\lambda_c = 450$ nm as a function of WO_3 top and bottom layers thickness for $CsFAPbI_3$ and $FAPbBr_3$ perovskite-based cells.

cells for comparison, where the PCE is reduced to 16.2% while AVT is increased to 22.5%, still higher than those reported in the literature using the same active material. Such high performances are obtained in a wide angular range up to about 50°, opposition to the typical device behavior in which performances decrease with the angle due to the higher intensity of back-reflected light. Moreover, LUEs of 4.3, 3.2, and 3.7% have been reached for $FAPbBr_3$, $CsFAPbI_3$, and $FAPbI_3$ devices, respectively, the highest so far achieved in unmixed perovskite solar cells. Regarding the other figures of merit, these devices show CRI values of 62, 80, and 92 and CIELab coordinates of (20.7, 41.4), (7.60, 4.80), and (2.88, 2.64), respectively, the last approaching neutrality color. All of these achievements show that DMD technology can have a huge impact in semitransparent perovskite solar cells.

Five different $WO_3/Ag/WO_3$ electrodes, with a fixed nominal Ag thickness of 14 nm (being the lower limit allowing for the best compromise between a good surface coverage and optical characteristics) and a dielectric thickness d ranging from 15 up to 70 nm have been realized: hereafter, for the sake of simplicity, the electrodes are labeled DMDd, with d = 15, 30, 40, 55, and 70 nm. We have studied their electromagnetic properties by VASE, consisting of analysis of the polarization change of the incident light after reflection from the sample. This change is characterized by ellipsometric phases, namely Ψ and Δ, related to the reflection coefficients $r_s = |r_s|e^{i\delta_s}$ and $r_p = |r_p|e^{i\delta_p}$ as follows: $\tan \Psi = |r_p|/|r_s|$ and $\Delta = \delta_p - \delta_s$ (see Figure 1a).[34]

In all devices with $d \geq 40$ nm, we find a critical angle of incidence θ_c and wavelength λ_c where Ψ approachs 90° (Figure 1b). In these conditions $r_s(\theta_c;\lambda_c) \cong 0$ or, in other words, the reflected light is fully p-polarized. The s and p modes of the reflected light for DMD40 at different angles are reported in Figure 1c, clearly showing that the s mode vanishes for θ_c = 46.30° and λ_c = 450 nm (see Figure S1 for the other devices). It is worth emphasizing that, contrary to the other configurations, the DMD40 electrode even shows a very low p mode reflection intensity at the same critical wavelength where the s mode vanishes, thus allowing for total antireflection conditions. This leads to very high transmittance values of >83% at around λ_c (Figure 1d). To understand the electromagnetic behavior of the realized devices, we extracted the optical dispersion of each layer in DMD configuration by fitting ellipsometric data with appropriate models (see the Experimental Methods and Figure S2). From VASE data, we

have extracted the real and imaginary parts ϵ_1 and ϵ_2 of the so-called complex pseudodielectric function $\langle\epsilon\rangle$,[38] expressing an averaged dielectric function of the full electrode. They are reported in Figure 2a as a function of wavelength for DMD40, 55, and 70 at critical angles.

It is clear that in all of the samples, the imaginary component ϵ_2 vanishes at the wavelength λ_c (see also Figures S1 and S3 for comparison), but only DMD40 displays a real dielectric function similar to that of air, namely $\epsilon_1(\lambda_c) \cong 1$ while for DMD55 and DMD70 $\epsilon_1(\lambda_c) \cong 2$ and $\epsilon_1(\lambda_c) \cong 10$, respectively. Therefore, DMD40 and air admittances perfectly match each other (see also the inset of Figure 1d).

Starting from this preliminary study, the p and s reflection mode coefficients, resulting from multireflection at the DMD interfaces, have been calculated by developing a phasor-reflected and transmitted light-field model. We emphasize that, so far, only the normal incidence condition has been analytically studied, besides with a low order of approximation,[32] while our model considers the propagation of light at any angle of incidence. In order to find analytical solutions, we assume that (i) both top and bottom WO_3 layers have the same thickness d and refractive index n and (ii) the real part of the Ag refractive index is negligible ($\tilde{n}_{Ag} \cong ik$), both assumptions being justified by the data reported in Figure S2. Under these assumptions, the reflectance (see the Supporting Information for more details) is

$$R \cong \frac{r_{12} + r_{23}e^{i2\delta_2} + r_{34}e^{i2(\delta_2+\delta_3)} + r_{12}r_{23}r_{34}e^{i2\delta_3}}{1 + r_{12}r_{23}e^{i2\delta_2} + r_{23}r_{34}e^{i2\delta_3} + r_{12}r_{34}e^{i2(\delta_2+\delta_3)}} \tag{1}$$

Here, r_{ik} are the Fresnel reflection mode coefficient amplitude between the ith and the kth layers while $\delta_k = \frac{2\pi}{\lambda}n_k d_k \cos \theta_k$ is the phase related to the optical path in the kth film where n_k, d_k, and θ_k are the refractive index, the thickness, and the angle of the propagation-ray in kth film, respectively. In order to validate this model, we plotted the achieved reflectance spectra at different angles of incident light, comparing them with the experimental curves of s and p modes derived by ellipsometric measurements. The good matching achieved between experiments and theory is shown in Figure S1 for DMD55 and 70 and in Figure S3 for DMD40.

Starting from these achievements, antireflection conditions ($R \cong 0$) lead to the follow analytical solution expressing the dielectric film thickness d as a function of the critical angle and critical wavelength of incidence light:
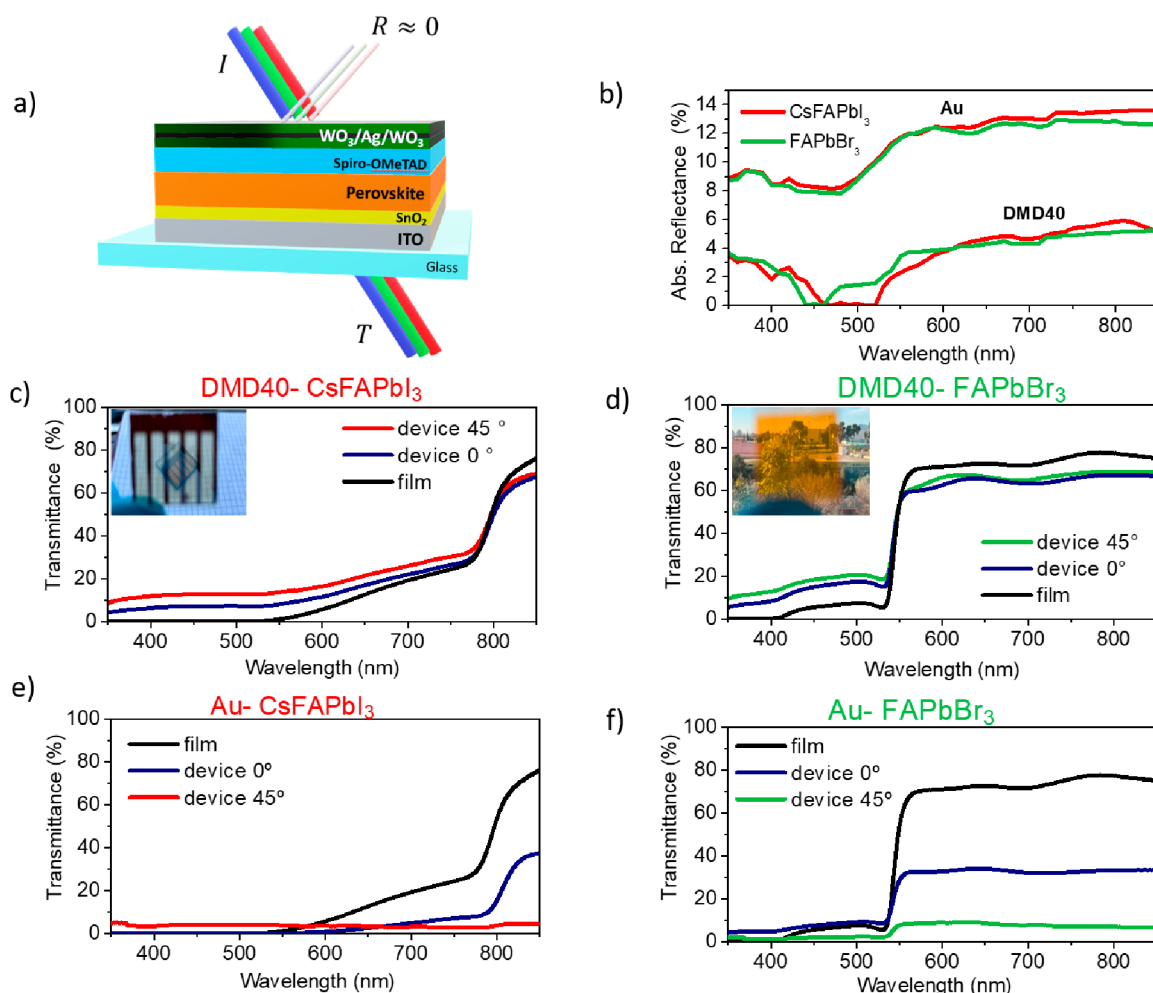
Figure 3. (a) Schematic of the STSC used in this work. (b) Absolute reflectance of DMD40-STSC and reference Au-STSC-based devices. (c,d) Transmittance spectra of a net film on glass and DMD40-STSC devices at normal incidence and 45° off-normal incidence. Inset: pictures of the full devices. (e,f) Transmittance spectra of a net film on glass and Au-STSC devices at normal incidence and 45° off-normal incidence.

$$d = \frac{\lambda_c}{2\pi} \frac{g(r,\varphi)}{\sqrt{n^2 - \sin^2 \theta_c}} \qquad (2)$$

where $g(r,\varphi)$ is an analytical functions of $r = r_{12}$ (see the Supporting Information for details) and $\varphi = \arctan\sqrt{\frac{k^2 + \sin^2\theta}{n^2 - \sin^2\theta}}$. Equation 2 is plotted in Figure S4 together with the experimental data. We underline that this is the first mathematical model reported for such structures at any angle of light incidence, thus allowing for rational design of DMD electrodes showing antireflection conditions in wide spectral and angular ranges. Solving eq 1, we have calculated the average visible reflectance (AVR), defined similarly to AVT but with a reflection spectrum $R(\lambda)$ replacing the transmittance one. In Figure 2b, the AVR intensity versus d at normal incidence of light is reported with experimental values of AVT, while in Figure S5 it is represented also as a function of the angle of incident light θ for both light incident from the DMD side and light incident from the substrate side considering two different substrates, namely, glass ($n = 1.5$) and organic material ($n = 1.7$). Clearly, a dielectric thickness of 40 nm allows one to achieve good antireflection conditions in a wide angular range regardless of the layer under the WO₃-bottom

and regardless of the side direction of incident light. Correspondingly, a maximum AVT is achieved at the same dielectric thickness with a remarkable value of 78% in the wavelength range between 370 and 780 nm. Such good performances are ascribed to a very low refractive index shown by the Ag layer in a wide wavelength range (about 0.13 between 350 and 1000 nm), compared to other metal layers such as Au (see Figure S6).[39] This results in better antireflection response for D/Ag/D electrodes, as reported in Figure S7, compared to D/Au/D ones.

Since the transmittance properties of the analyzed electrodes make them extremely appealing to increase the overall performance characteristics of STSC devices, we have used the DMD40 as the top electrode in perovskite solar cells with the following architecture: ITO/SnO₂/perovskite/spiro-OMe-TAD/top electrode, making a comparison with reference devices based on a 30 nm thick Au electrode.[40−42] To check the impact of the full cell structure on the antireflection conditions, we performed optical simulations of light reflectance intensity maps as a function of the dielectric thicknesses, as reported in Figure 2c. As it is clear, the best thickness compromise for WO₃ layer thickness is still around 40 nm, as already observed for DMD deposited on glass (Figure 2b), thus proving that the organic and perovskite
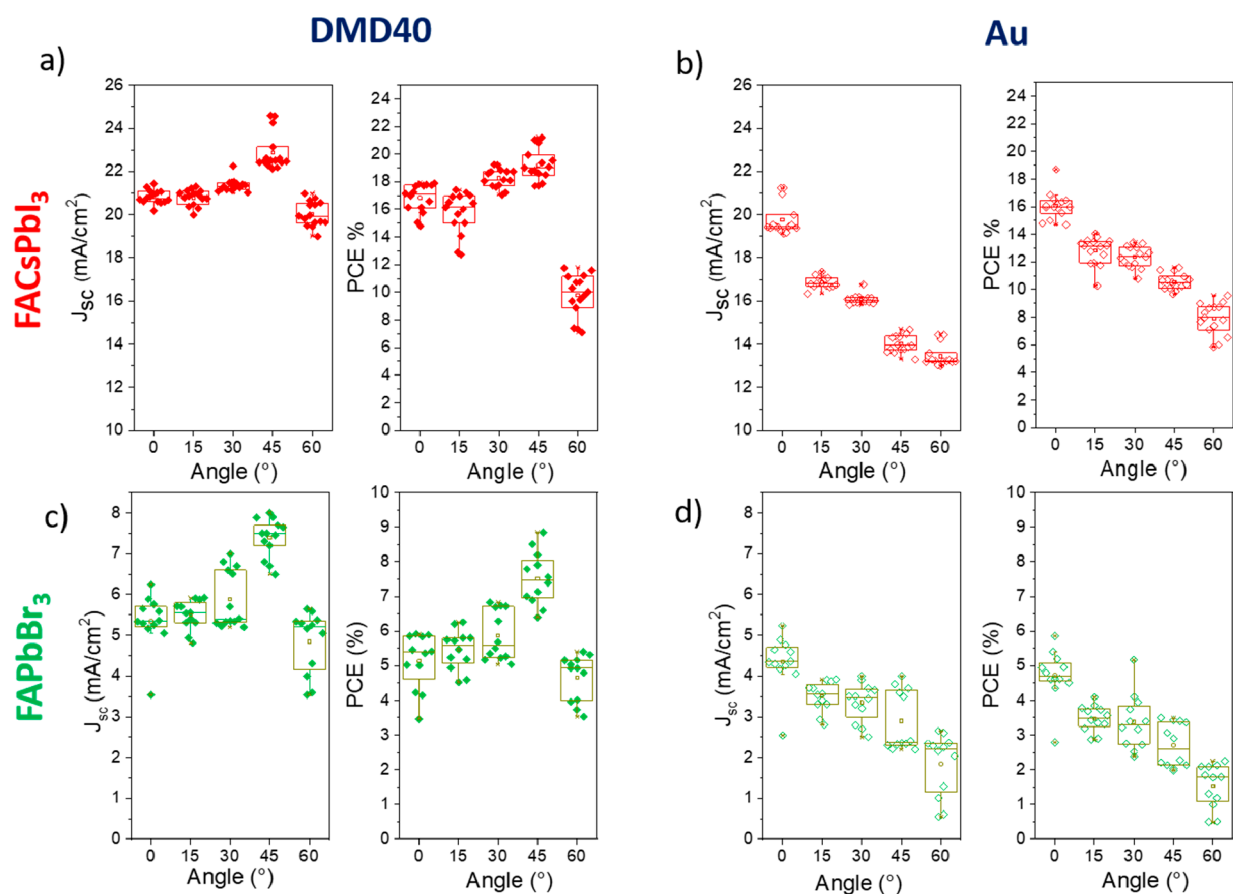
Figure 4. Statistical distribution of J_{sc} and PCE data vs the light incident angle of CsFAPbI$_3$ (red data) and FAPbBr$_3$ (green data) devices with the DMD40 electrode (a,c) and Au (b,d).

underlayer interfaces do not modify the antireflection conditions. This is further confirmed by observing that the regions corresponding to the minimum reflectance in the maps of Figure 2c have the same shape. The reason is that higher-order contributions, such as r_{45}, namely, the reflection at the WO$_3$-bottom/underlayer interface (WO$_3$/glass or, in the case of the solar cell, WO$_3$/organic), are negligible with respect to r_{12} (air/WO$_3$-top), r_{23} (WO$_3$-top/Ag), and r_{34} (Ag/WO$_3$-bottom) because the transmitted light is attenuated by the reflection at each interface of the upper layers, antireflection conditions being mainly due to the disruptive interference between r_{23}, r_{34}, and r_{12} phasors (see the Supporting Information).

A scheme of the realized devices is reported in Figure 3a, while the X-ray diffraction spectra of perovskite layers and the SEM cross section images of the devices are reported in Figures S8 and S9, respectively. In Figure 3b, the absolute reflectance of both Au and DMD40-based STSC devices has been reported, showing a value ranging between about 8 and 14% for the former and less than about 5% for the latter, with negligible reflection values around the critical wavelength (450 nm). The transmittance spectra of neat films and of DMD40-STSC devices have been reported at normal incidence and 45° off-normal incidence in Figure 3c,d for CsFAPbI$_3$ and FAPbBr$_3$, respectively, clearly showing in both cases an improvement of transmittance in the range where the DMD reflectance is minimized. The transmittance spectra of reference devices with Au have been also reported (Figure 3e,f) for comparison, showing a reduction with the light

incident angle due to the higher intensity of back-reflected light.

We attribute this improvement to solely the antireflection conditions reached by the DMD electrode, as shown by the diffused reflectance (see Figure S10, where we also reported the photon-balance check curves for all of the devices realized in this work). The short-current density J_{sc} and PCE versus the angle of incidence of light are reported in Figure 4 for the overall realized devices. While the Au-based STSC devices show a reduction of the overall performances with increasing angle of incident light, on the contrary, the DMD40-based ones display an increase of the overall values up to the critical angle, then rolling off mainly because of the increasing reflection intensity, as reported in Figure 1c. It must be remarked that at 45° relative increases of 73 and 200% in PCE for CsFAPbI$_3$ and FAPbBr$_3$, respectively, have been obtained compared to the relative Au reference devices, thus resulting in 80 and 50 W of electrical power gained for each square meter reached by solar peak radiation. The open-circuit voltage, V_{oC}, and fill factor, FF, for each of the devices at the different angles are reported in Figures S11 and S12, showing no remarkable differences between DMD40 and Au reference devices. This demonstrates that the DMD40 electrode is efficient and stable (as well as Au) to extract the electric charges produced by the photoabsorption process, as reported also in Figure S13 for time stability measurement of the maximum power point current and Figure S14 and Table S1 for the hysteresis. In Figure S15, we reported the V_{oC}, J_{sc}, and FF versus AVT of the devices reported in this work, compared with literature,[43,44]
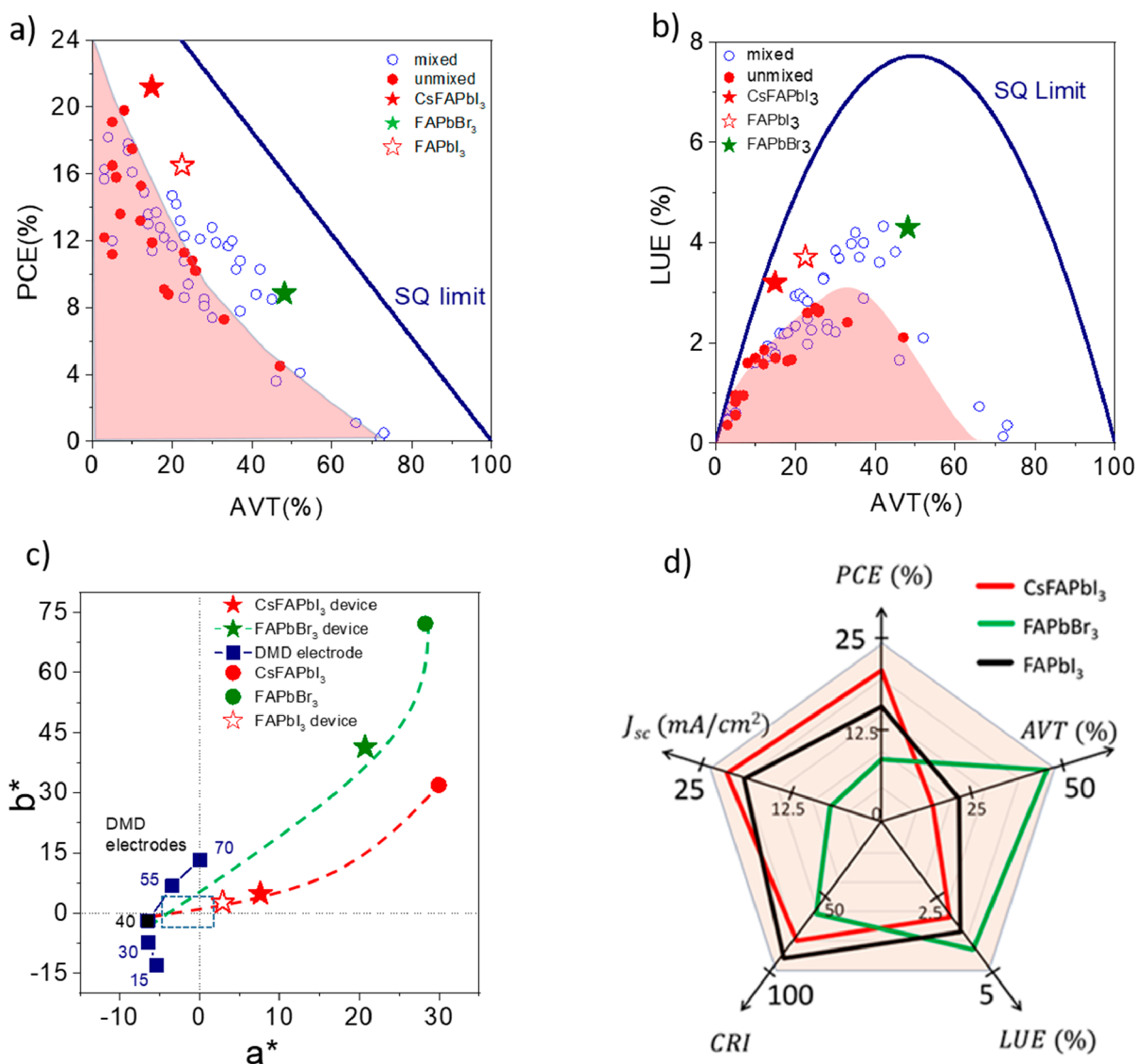
Figure 5. PCE (a) and LUE (b) vs AVT of realized devices compared with the literature [see refs 43 and 44]. (c) Chromaticity coordinates CIELab for the net perovskite, DMD electrodes, and solar cell devices. The rectangular area is the coordinate range accepted for window applications. (d) Polar diagram of best operation performances achieved by DMD40 perovskite STSCs.

from which emerged that good optical performances of the DMD-based devices are reached without detriment of the electrical ones.

The PCE and LUE versus AVT data are shown in Figure 5a,b, respectively, for the DMD40-STSC devices at 45° off-normal incidence (star-like dots) compared with the overall no-wavelength-selective-STSC so far reported in the literature,[43,44] together with the SQ limit curves (red and blue dots represent the data from literature related to unmixed and mixed perovskite STSCs). As we can see, the devices reported in this work outperform the values shown up to now in the literature for the corresponding AVT.

In more detail, the DMD40-CsFAPbI$_3$ device shows a PCE of 21.2% at an AVT value of 15% while the DMD40-FAPbBr$_3$ device reaches a PCE value of about 8.9% at an AVT of 48.1%. In pure FAPbI$_3$-based cells, although PCE decreases to 16.2%, AVT increases up to 22.5%, still higher than those reported in the literature for the same material-based devices.[43,44] This is mirrored in LUE values that are 3.2, 3.7, and 4.3% for CsFAPbI$_3$, FAPbI$_3$, and FAPbBr$_3$ best devices, respectively,

such values being the highest so far achieved for the corresponding AVT. Concerning the other figures of merit, the CsFAPbI$_3$ device shows a CRI value of 80 and CIELab coordinates of (+7.6, +4.8), among the best reported in the literature so far,[31] while for the FAPbBr$_3$ device, a CRI of about 62 and a*, b* of (+20.7, +41.4) are obtained, useful for agrivoltaic applications. Such values are even better in the case of pure FAPbI$_3$ reaching CRI = 92 and CIELab of (+2.9, +2.6), very near achieving neutral color appearance. We remark that the net perovskite films display CIELab coordinates of about (+29.9, +31.9) for CsFAPbI$_3$ and (+28.7, +77.2) for FAPbBr$_3$.

Therefore, the CIELab coordinates shown by the corresponding DMD40 devices result in being much lower than those of the net films due to a compensation effect produced by the negative CIELab values displayed by the DMD40 electrode solely, namely, (−6.5, −2.0), that cannot be reached by the D/Au/D electrode, due to the optical dispersion of the Au metal layer (see Figure S6). Moreover, the change in the CIExy coordinates is very low, ranging from (0.40, 0.35) at 0° to (0.37, 0.35) at 45° (a variation of less than 0.03) and from

(0.46, 0.41) at 0° to (0.45, 0.40) at 45° (a variation of less than 0.01) for CsFAPbI$_3$ and FAPbBr$_3$, respectively, thus demonstrating negligible color variation between normal and off-angle.[5] A review of the overall maximum operation performances of the overall DMD40-based STSC devices is reported in Figure 5d.

In summary, unprecedented single-junction STSC devices have been fabricated thanks to rational management of the light reflection modes of a dielectric/metal/dielectric triple layer used as the top electrode. This approach allows for an increase in the overall characteristics of the devices for different types of perovskite thin-film materials. This technology may be important, especially for PV devices integrated in buildings where light from the sun does not necessarily strike perpendicularly to the irradiated surface. For example, in a north-average latitude of 45°, the sun maximum altitude oscillates between 68.5 and 21.5° in the summer and winter solstice, respectively. Therefore, a photovoltaic window based on such an antireflecting DMD electrode exposed to the south would be a competitive technology for producing sustainable greenhouse-free energy or for agrivoltaic applications where the neutrality of color of the semitransparent cells is not indispensable. Since our strategy is not dependent on the active layer used, a further increment of such performances could be achieved by mixing different halide-based perovskites or organic materials to tune the absorption spectrum of the active layer.[45] Moreover, we emphasize that our approach is universal as it can be extended to several DMD materials and optoelectronic device applications, including infrared perovskite solar cells[43] and tandem architectures.[45−48] Antireflection coatings such as MgF$_2$ are widely used in photovoltaic devices.[49] By contrast, the DMD architecture offers the advantage to conduct carriers, allowing one also to obtain bifacial semitransparent solar cells with high reproducible results. Nevertheless, MgF$_2$ is compatible with our technology as an antireflection coating at the air−glass side interface, where typically more than 5% of light is reflected back. Finally, although beyond the scope of this work, a deep study regarding the environmental advantage gained by the substitution of gold in the new electrode would be also of interest for practical applications.

ASSOCIATED CONTENT

Supporting Information

The Supporting Information is available free of charge at https://pubs.acs.org/doi/10.1021/acsenergylett.3c02602.

Detailed description of the experimental methods, including synthesis, film deposition, device fabrication, and characterization, additional data and figures, and the theoretical model (PDF)

AUTHOR INFORMATION

Corresponding Authors

Sofia Masi − Institute of Advanced Materials (INAM), Universidad Jaume I, 12071 Castelló, Spain; orcid.org/0000-0002-7373-1627; Email: masi@uji.es

Stefano De Leo − Department of Applied Mathematics, Campinas State University, 13083-859 São Paulo, Brazil; Email: deleo@ime.unicamp.br

Marco Mazzeo − Department of Mathematics and Physics "Ennio De Giorgi", University of Salento, 73100 Lecce, Italy; CNR NANOTEC-Institute of Nanotechnology, 73100 Lecce,

Italy; orcid.org/0000-0001-5401-801X; Email: marco.mazzeo@unisalento.it

Authors

Antonella Lorusso − Department of Mathematics and Physics "Ennio De Giorgi", University of Salento, 73100 Lecce, Italy; CNR NANOTEC-Institute of Nanotechnology, 73100 Lecce, Italy

Claudia Triolo − Department of Civil, Energy, Environmental and Materials Engineering (DICEAM), Mediterranean University, 89122 Reggio Calabria, Italy

Fabrizio Mariano − CNR NANOTEC-Institute of Nanotechnology, 73100 Lecce, Italy

Simone Muia − Department of Mathematics and Physics "Ennio De Giorgi", University of Salento, 73100 Lecce, Italy

Alessandro Cannavale − Dipartimento di Architettura, Costruzione e Design (ArCoD), Politecnico di Bari, 70125 Bari, Italy

Yu Duan − State Key Laboratory on Integrated Optoelectronics, College of Electronic Science & Engineering, Jilin University, Changchun 130012, P. R. China; orcid.org/0000-0002-2155-7188

Marco Anni − Department of Mathematics and Physics "Ennio De Giorgi", University of Salento, 73100 Lecce, Italy; orcid.org/0000-0002-1651-0166

Maria Luisa De Giorgi − Department of Mathematics and Physics "Ennio De Giorgi", University of Salento, 73100 Lecce, Italy; orcid.org/0000-0002-3774-6477

Salvatore Patané − Department of Mathematical and Computer Sciences, Physical Sciences and Earth Sciences, University of Messina, 98166 Messina, Italy; orcid.org/0000-0003-2517-0236

Olfa Selmi − Institute of Advanced Materials (INAM), Universidad Jaume I, 12071 Castelló, Spain

Iván Mora-Seró − Institute of Advanced Materials (INAM), Universidad Jaume I, 12071 Castelló, Spain; orcid.org/0000-0003-2508-0994

Complete contact information is available at: https://pubs.acs.org/10.1021/acsenergylett.3c02602

Notes

The authors declare no competing financial interest.

REFERENCES

(1) Jeong, J.; Kim, M.; Seo, J.; Lu, H.; Ahlawat, P.; Mishara, A.; Yang, Y.; Hope, M. A.; Eickemeyer, F. T.; Kim, M.; et al. Pseudo-Halide Anion Engineering for α-FAPbI3 Perovskite Solar Cells. Nature 2021, 592, 381−385.

(2) Zhao, Y.; Ma, F.; Qu, Z.; Yu, S.; Shen, T.; Deng, H. X.; Chu, X.; Peng, X.; Yuan, Y.; Zhang, X.; You, J. Inactive (PbI2)2RbCl Stabilizes Perovskite Films for Efficient Solar Cells. *Science* **2022**, *377*, 531−534.

(3) Giuliano, G.; Bonasera, A.; Arrabito, G.; Pignataro, B. Semitransparent Perovskite Solar Cells for Building Integration and Tandem Photovoltaics: Design Strategies and Challenges. *Sol. RRL* **2021**, *5*, 2100702.

(4) Rahmany, S.; Etgar, L. Semitransparent Perovskite Solar Cells. *ACS Energy Lett.* **2020**, *5*, 1519−1531.

(5) Traverse, C. J.; Pandey, R.; Barr, M. C.; Lunt, R. R. Emergence of Highly Transparent Photovoltaics for Distributed Applications. *Nat. Energy* **2017**, *2*, 849−860.

(6) Thompson, E. P.; Bombelli, E. L.; Shubham, S.; Watson, H.; Everard, A.; D'Ardes, V.; Schievano, A.; Bocchi, S.; Zand, N.; Howe, C. J.; Bombelli, P. Tinted Semi-Transparent Solar Panels Allow Concurrent Production of Crops and Electricity on the Same Cropland. *Adv. Energy Mater.* **2020**, *10*, 2001189.

(7) Yang, C.; Liu, D.; Bates, M.; Barr, M. C.; Lunt, R. R. How to Accurately Report Transparent Solar Cells. *Joule* **2019**, *3*, 1803−1809.

(8) Yuan, L.; Wang, Z.; Duan, R.; Huang, P.; Zhang, K.; Chen, Q.; Allam, N. K.; Zhou, Y.; Song, B.; Li, Y. Semi-Transparent Perovskite Solar Cells: Unveiling the Trade-Off between Transparency and Efficiency. *J. Mater. Chem. A* **2018**, *6*, 19696−19702.

(9) Shockley, W.; Queisser, H. J. Detailed Balance Limit of Efficiency of p-n Junction Solar Cells. *J. Appl. Phys.* **1961**, *32*, 510−519.

(10) Eperon, G. E.; Burlakov, V. M.; Goriely, A.; Snaith, H. J. Neutral color semitransparent microstructured perovskite solar cells. *ACS Nano* **2014**, *8*, 591−598.

(11) Chen, W.; Zhang, J.; Xu, G.; Xue, R.; Li, Y.; Zhou, Y.; Hou, J.; Li, Y. A Semitransparent Inorganic Perovskite Film for Overcoming Ultraviolet Light Instability of Organic Solar Cells and Achieving 14.03% Efficiency. *Adv. Mater.* **2018**, *30*, 1800855.

(12) Kim, H. B.; Choi, H.; Jeong, J.; Kim, S.; Walker, B.; Song, S.; Kim, J. Y. Mixed Solvents for the Optimization of Morphology in Solution-Processed, Inverted-Type Perovskite/Fullerene Hybrid Solar Cells. *Nanoscale* **2014**, *6*, 6679−6683.

(13) Bag, S.; Durstock, M. F. Efficient Semi-Transparent Planar Perovskite Solar Cells Using a 'Molecular Glue'. *Nano Energy* **2016**, *30*, 542−548.

(14) Mariano, F.; Cretì, A.; Carbone, L.; Genco, A.; D'Agostino, S.; Carallo, S.; Montagna, G.; Lomascolo, M.; Mazzeo, M. The enhancement of excitonic emission crossing Saha equilibrium in trap passivated CH3NH3PbBr3 perovskite. *Comm. Phys.* **2020**, *3*, 1−10.

(15) Park, H.; Chang, S.; Smith, M.; Gradecak, S.; Kong, J. Interface Engineering of Graphene for Universal Applications as both Anode and Cathode in Organic Photovoltaics. *Sci. Rep* **2013**, *3*, 1581.

(16) Zhang, Z. K.; Du, J.; Zhang, D.; Sun, H.; Yin, L.; Ma, L.; Chen, J.; Ma, D.; Cheng, H. M.; Ren, W. Rosin-enabled ultraclean and damage-free transfer of graphene for large-area flexible organic light-emitting diodes. *Nat. Commun.* **2017**, *8*, 14560.

(17) Lee, S.; Jang, J.; Park, T.; Park, Y. M.; Park, J. S.; Kim, Y. K.; Lee, H. K.; Jeon, E. C.; Lee, D. K.; Ahn, B.; Chung, C. H. Electrodeposited Silver Nanowire Transparent Conducting Electrodes for Thin-Film Solar Cells. *ACS Appl. Mater. Interfaces* **2020**, *12*, 6169−6175.

(18) Ahn, J.; Hwang, H.; Jeong, S.; Moon, J. Metal-Nanowire-Electrode-Based Perovskite Solar Cells: Challenging Issues and New Opportunities. *Adv. Energy Mater.* **2017**, *7*, 1602751.

(19) Wang, J.; Meng, C.; Liu, H.; Hu, Y.; Zhao, L.; Wang, W.; Xu, X.; Zhang, Y.; Yan, H. Application of Indium Tin Oxide/Aluminum-Doped Zinc Oxide Transparent Conductive Oxide Stack Films in Silicon Heterojunction Solar Cells. *ACS Appl. Energy Mater.* **2021**, *4*, 13586−13592.

(20) Choi, S.; Zhou, Y.; Haske, W.; Shim, J. W.; Fuentes-Hernandez, C.; Kippelen, B. ITO-Free Large-Area Flexible Organic Solar Cells with an Embedded Metal Grid. *Org. Electron.* **2015**, *17*, 349−354.

(21) Lu, S.; Sun, Y.; Ren, K.; Liu, K.; Wang, Z.; Qu, S. Recent Development in ITO-free Flexible Polymer Solar Cells. *Polymers* **2018**, *10*, 5.

(22) Bush, K. A.; Bailie, C. D.; Chen, Y.; Bowring, A. R.; Wang, W.; Ma, W.; Leijtens, T.; Moghadam, F.; McGehee, M. D. Thermal and Environmental Stability of Semi-Transparent Perovskite Solar Cells for Tandems Enabled by a Solution-Processed Nanoparticle Buffer Layer and Sputtered ITO ElectrodeElectrode. *Adv. Mater.* **2016**, *28*, 3937−3943.

(23) Yoon, S.; Ha, H. U.; Seok, H.; Kim, H.; Kang, D. Highly Efficient and Reliable Semitransparent Perovskite Solar Cells via Top Electrode Engineering. *Adv. Funct. Mater.* **2022**, *32*, 2111760.

(24) Bett, A. J.; Winkler, K. M.; Bivour, M.; Cojocaru, L.; Kabakli, O. S.; Schulze, P. S. C.; Siefer, G.; Tutsch, L.; Hermle, M.; Glunz, S. W.; Goldschmidt, J. C. Semi-Transparent Perovskite Sola Cells with ITO Directly Sputtered on Spiro-OMeTAD for Tandem Applications. *ACS Appl. Mater. Interfaces* **2019**, *11*, 45796−45804.

(25) Xie, X.; Wu, C.; Sun, S.; Xu, X.; Xu, W.; Qin, G.; Xiao, L. Semitransparent Perovskite Solar Cells with Dielectric/Metal/Dielectric Top Electrodes. *Energy Technol.* **2020**, *8*, 1900868.

(26) Lee, S.; Choi, C. S.; Choi, K. C.; Lee, H. Low resistive transparent and flexible ZnO/Ag/ZnO/Ag/WO3 electrode for organic light-emitting diodes. *Org. Electron.* **2012**, *13*, 1654−1659.

(27) Lucarelli, G.; Brown, T. M. Development of Highly Bendable Transparent Window Electrodes Based on MoOx, SnO2, and Au Dielectric/Metal/Dielectric Stacks: Application to Indium Tin Oxide (ITO)-Free Perovskite Solar Cells. *Front. Mater.* **2019**, *6*, 310.

(28) Cherif, M. A.; Labiod, A.; Barakel, D.; Touihri, S.; Torchio, P. Tailored ZnS/Ag/TiOx transparent and conductive electrode for organic solar cells. *EPJ. Photovoltaics* **2019**, *10*, 2.

(29) Yin, Y.; Lan, C.; Guo, H.; Li, C. Reactive Sputter Deposition of WO3/Ag/WO3 Film for Indium Tin Oxide (ITO)-Free Electrochromic Devices. *ACS Appl. Mater. Interfaces* **2016**, *8*, 3861−3867.

(30) Hong, K.; Kim, K.; Kim, S.; Lee, I.; Cho, H.; Yoo, S.; Choi, H. W.; Lee, N. Y.; Tak, Y. H.; Lee, J. L. Optical Properties of WO3/Ag/WO3Multi layer As Transparent Cathode in Top-Emitting Organic Light Emitting Diodes. *J. Phys. Chem. C* **2011**, *115*, 3453−3459.

(31) Yu, J. C.; Li, B.; Dunn, C. J.; Yan, J.; Diroll, B. T.; Chesman, A. S. R.; Jasieniak, J. J. High-Performance and Stable Semi-Transparent Perovskite Solar Cells through Composition Engineering. *Adv. Sci.* **2022**, *9*, 2201487.

(32) Ji, C.; Liu, D.; Zhang, C.; Guo, L. J. Ultrathin-Metal-Film-Based Transparent Electrodes with Relative Transmittance Surpassing 100%. *Nat. Commun.* **2020**, *11*, 3367.

(33) D'Ercole, D.; Dominici, L.; Brown, T. M.; Michelotti, F.; Reale, A.; Di Carlo, A. Angular response of dye solar cells to solar and spectrally resolved light. *Appl. Phys. Lett.* **2011**, *99*, 213301.

(34) Fujiwara, H. Spectroscopic Ellipsometry: Principles and Applications; Wiley Online Library, 2007.

(35) Cattin, L.; Louarn, G.; Morsli, M.; Bernede, J. C. Semi-Transparent Organic Photovoltaic Cells with Dielectric/Metal/Dielectric Top Electrode: Influence of the Metal on Their Performances. *Nanomaterials* **2021**, *11*, 393.

(36) Wang, Y.; He, B.; Wang, H.; Xu, J.; Ta, T.; Li, W.; Wang, Q.; Yang, S.; Tang, Y.; Zou, B. Transparent $WO_3/Ag/WO_3$ Electrode for Flexible Organic Solar Cells. *Mater. Lett.* **2017**, *188*, 107−110.

(37) Tao, C.; Ruan, S.; Xie, G.; Kong, X.; Shen, L.; Meng, F.; Liu, C.; Zhang, X.; Dong, W.; Chen, W. Role of Tungsten Oxide in Inverted Polymer Solar Cells. *Appl. Phys. Lett.* **2009**, *94*, 043311.

(38) Yang, H. U.; D'Archangel, J.; Sundheimer, M. L.; Tucker, E.; Boreman, G. D.; Raschke, M. B. Optical Dielectric Function of Silver. *Phys. Rev. B* **2015**, *91*, 235137.

(39) Kim, J.; Kim, D.; Kim, W.; Woo, S.; Baek, S.; Ko, M. J.; Kim, Y. Efficient Semi-Transparent Perovskite Quantum Dot Photovoltaics Enabled by Asymmetric Dielectric/Metal/Dielectric Transparent Electrodes. *Chem. Eng. J.* **2023**, *469*, 143824.

(40) Salim, K. M. M.; Masi, S.; Gualdron-Reyes, A. F.; Sanchez, R. S.; Barea, E. M.; Krecmarova, M.; Sanchez-Royo, J. F.; Mora-Sero, I. Boosting long-term stability of pure formamidinium perovskite solar

cells by ambient air additive assisted fabrication. *ACS Energy Lett.* **2021**, *6*, 3511−3521.

(41) Lie, S.; Bruno, A.; Wong, L. H.; Etgar, L. Semitransparent Perovskite Solar Cells with > 13% Efficiency and 27% Transperancy Using Plasmonic Au Nanorods. *ACS Appl. Mater. Interfaces* **2022**, *14*, 11339−11349.

(42) Masi, S.; Gualdrón-Reyes, A. F.; Mora-Seró, I. Stabilization of Black Perovskite Phase in FAPbI3 and CsPbI3. *ACS Energy Lett.* **2020**, *5*, 1974−1985.

(43) Almora, O.; Baran, D.; Bazan, G. C.; Berger, C.; Cabrera, C. I.; Catchpole, K. R.; Erten-Ela, S.; Guo, F.; Hauch, J.; Ho-Baillie, A. W. Y.; et al. Device Performance of Emerging Photovoltaic Materials. *Adv. Energy Mater.* **2021**, *11*, 2002774.

(44) Almora, O.; Baran, D.; Bazan, G. C.; Cabrera, C. I.; Erten-Ela, S.; Forberich, K.; Guo, F.; Hauch, J.; Ho-Baillie, A. W. Y.; Jacobsson, T. J.; et al. Device Performance of Emerging Photovoltaic Materials (Version 3). *Adv. Energy Mater.* **2023**, *13*, 2203313.

(45) Zuo, L.; Shi, X.; Fu, W.; Jen, A. K. Y. Highly Efficient Semitransparent Solar Cells with Selective Absorption and Tandem Architecture. *Adv. Mater.* **2019**, *31*, 1901683.

(46) Fu, F.; Feurer, T.; Weiss, T. P.; Pisoni, S.; Avancini, E.; Andres, C.; Buecheler, S.; Tiwari, A. N. High-Efficiency Inverted Semi-Transparent Planar Perovskite Solar Cells in Substrate Configuration. *Nat. Energy* **2017**, *2*, 16190.

(47) Park, H. H. Transparent Electrode Techniques for Semi-transparent and Tandem Perovskite Solar Cells. *Electr. Mater. Lett.* **2021**, *17*, 18−32.

(48) Bush, K.; Palmstrom, A.; Yu, Z.; Boccard, M.; Cheacharoen, R.; Mailoa, J.; McMeekin, D.; Hoye, R.; Bailie, C.; Leijtens, T.; et al. 23.6%-Efficient Monolithic Perovskite/Silicon Tandem Solar Cells with Improved Stability. *Nat. Energy* **2017**, *2*, 17009.

(49) Jung, S. K.; Park, K.; Lee, D. K.; Lee, J. H.; Ahn, H.; Lee, J. W. Effects of MgF2 anti-reflection coating on optical losses in metal halide perovskite solar cells. *Nanotechnology* **2024**, *35*, 135401.